SEECCM III
3rd South-East European Conference on Computational Mechanics-
an ECCOMAS and IACM Special Interest Conference
M. Papadrakakis, M. Kojic, I. Tuncer (eds.)
Kos Island, Greece, 12–14 June 2013

NUMERICAL INVESTIGATION OF A FULL-SCALE RC BRIDGE THROUGH 3D DETAILED NONLINEAR LIMIT-STATE SIMULATIONS

George Markou

Department of Civil Engineering, Alhosn University, Abu Dhabi, UAE
P.O.Box 38772, Abu Dhabi
g.markou@alhosnu.ae

Keywords: Bridge Modeling, Large-Scale Simulations, Nonlinear Analysis.

Abstract. *In this paper, a numerical investigation of the computational performance of ReConAn FEA will be performed through the full-scale 3D detailed modeling of a 100m span reinforced concrete bridge. The efficiency of the automatic procedure for generating embedded steel reinforcement elements inside the hexahedral finite elements will be presented and the numerical performance of the solver will be discussed. Furthermore, the numerical results that derived from the nonlinear numerical assessment of the bridge will be analyzed where a simplified finite element model developed in SAP2000 was used to compare the derived results from the 3D detailed simulation. In the 3D detailed modeling formulation adopted in this work, concrete is modeled through the use of 8-noded hexahedral elements that treat the cracking phenomenon through the smear crack approach and the reinforcement is modeled through the use of embedded 2-noded rod elements that incorporate the Menegotto-Pinto steel material model. The rebars are assumed to have perfect bonding thus the bond-slip between the rebars and concrete depends on failure of the concrete material. The piers with the pile cap and the bridge's trapezoidal shaped continuous deck are modeled through the use of the adopted concrete hexahedral element, while the 3D geometry of the reinforcement grid, inside the concrete domain, is modeled in detail according to the technical drawings. Finally, the elastomeric bearings are also modeled by using 8-noded hexahedral elements that discretize the exact geometry of the isolation system.*

1 INTRODUCTION

Modeling and analysis of reinforced concrete (RC) bridges has been a scientific topic that challenged and still challenges researchers and finite element (FE) software developers that deal with the assessment of the mechanical behavior of RC bridges in terms of ductility and maximum capacity. Allocating potential weaknesses in the design that derives from the complexity of the bridges' geometry is a difficult procedure given that implementing detailed modeling for this type of structures is usually a prohibitive numerical task due to the large-scale numerical models that derive during the analysis procedure. Nevertheless, it is indisputable that 3D detailed FE models derive the most accurate numerical results in terms of objectivity.

In order to assess the mechanical behavior of RC bridges under earthquake loads according to Eurocode [1] or AASHTO [2] provisions, several methods have been proposed the last three decades, which mainly involve three procedures: modal pushover analysis, linear dynamic analysis and linear static analysis [3]. Most researchers [4-18] study the mechanical behavior of bridge structures through the use of beam-column and 2D FEs (i.e. the shell FE), which gives them the ability, through simplification assumptions related to both material and geometrical features, to investigate the overall dynamic and nonlinear behavior of the under study RC structures for different types of load magnitudes. The simplified models provide the required numerical tools to study the overall behavior at the full-scale structural level but lack in providing the researchers with the ability to account localized nonlinear phenomena like cracking, reinforcement geometry, yielding of rebars, 3D mechanical behavior of elastomeric bearings and their interaction with the deck, piers and abutments, etc., thus having non-negligible effects on the numerical results and the overall mechanical behavior of the bridges that derive from this type of analysis models.

As it was stated in [14], the last two decades the scientists and practitioners shifted towards the performance based assessment and design concept, where the inelastic deformation demands derive directly from the numerical nonlinearities that are incorporated and used during the nonlinear analysis. This emphasizes the need of accurate nonlinear models that will be able to account for 3D nonlinearities and phenomena that result from both material and geometrical features of the under study structures. For this reason, several researchers began to lean towards the 2D [19, 20] and eventually 3D detailed modeling of independent structural members of the bridge [21-29]. Furthermore, scientists managed to model the complete structural geometry of bridges [30-36], in an attempt to address the above issue.

Mwafy et al. [35], propose an idealization methodology that foresees the modeling through SAP2000 [37] and Zeus NL [38] of the super-structure of the bridge A-1700 at Caruthersville, with beam-column elements and the sub-structure with cubic elasto-plastic elements, including the soil domain in their numerical model. The focus on describing a realistic idealization procedure in this research work [35] stresses the significance of having the ability to simulate large-scale structures through the use of 3D detailed models that account material nonlinearities, while the computational constraints that result when this type of modeling is adopted relates with the inability of standard computer systems to undertake such a numerical task.

Richard et al. [19] used ATENA software [39] to analyze a 50 years old concrete trough bridge through the use of a 2D finite element model that treats cracking through the use of the smeared crack approach and models the reinforcement with embedded truss elements. Their idealization assumption was also restraint by the computational demands that would have resulted if a full-scale 3D finite element model was constructed.

Tang and Hao [34], used 3D detailed modeling in specific structural parts of a cable-stayed bridge in order to simulate the mechanical behavior of RC in blast loads and then assess the

overall mechanical response of the bridge due to the loss of the carrying capacity of these structural members, through the use of less computational demanding FE models (beam and shell elements). The simulations that were performed in LS-DYNA [40], showed that the computational demand was excessive, even for the case of the numerical analysis of a single pier. It is important to note here that in this study the bond-slip between the steel reinforcement and concrete is accounted as a property of concrete failure. The same assumption was also made in [25, 27, 33, 41] and it is the approach that the current research work will adopt during the numerical analysis.

Bi and Hao [33] used LS-DYNA to construct a full-scale 3D model of a two-span RC bridge with a straight deck (total span of 60m) in order to study the pounding damage under spatial varying ground motions. The idealization procedure adopted in this study foreseen the use of solid concrete elements with embedded rebars near the pounding areas, while smeared models (reinforcement is assumed to be equally distributed over concrete elements), away from the pounding regions, were used in order to minimize the computational demand. The RC bridge consisted of eight unreinforced elastomeric bearing pads, which were modeled with 16 solid finite elements each.

Other commercial software can be also found in the international literature that were used to assess the mechanical behavior of RC bridge structures. Deng and Morcous [29], Chacon and Mirambell [28], Frissen et al. [21], Zhou et al. [13], Johnson et al. [8], Kaviani et al. [12] and Ho et al. (GT STRUDL Technical Papers) [42], used ANSYS [43], ABAQUS [44], TNO DIANA [45], Strand7 [46], Drain 3DX [47], Opensees [48], ADINA [49] and GT STRUDL [42], respectively, so as to numerically assess RC bridges through the use of different FE models. Commercial software that are referenced in [42-49] have the ability of using 3D FE models that incorporate damage material models. Given the fact that modeling RC structures through the use of 3D detailed FE models that incorporate cracking propagation through the smeared approach and model the reinforcement with embedded rebar elements [50-58], is computationally challenging even for relatively small models, none of the referenced commercial and research software were used to model a full-scale RC bridge and perform a seismic assessment through push over analysis.

In this paper the full-scale modeling of a 100m span RC bridge with an arc-shaped deck will be performed by using ReConAn FEA research software [59]. The preliminary design is assessed by performing pushover analysis, while the numerical results are compared with the results that derive from a simplified model developed in SAP2000, which is also used to perform modal analysis. In the 3D detailed modeling formulation adopted in this work, concrete is discretized through the use of the 8-noded hexahedral element that accounts the cracking phenomenon through the smear crack approach. The reinforcement is modeled through the use of embedded 2-noded rod elements, which are assumed to have perfect bonding with concrete elements. The piers with the pile cap and the bridge's trapezoidal shaped continuous deck are modeled through the use of the adopted concrete hexahedral element, while the 3D geometry of the reinforcement grid, inside the concrete domain, is modeled in detail according to the preliminary technical drawings. The elastomeric bearings are also modeled in detailed by using 8-noded hexahedral elements that discretize the exact geometry of the isolation system. So as to investigate the numerical response of the adopted model for simulating the mechanical behavior of the isolation system, a parametric investigation is performed. Finally, explicit modeling of the posttensioning system is developed and numerically investigated. After the construction of the complete detailed model, the seismic assessment of the RC bridge is presented.

2 GEOMETRY OF THE BRIDGE

As it is described in [60] the bridge has an effective span of 99.1 m, of which 51.55 m is the left span's length and 47.55 m is the right span's length. The total height of the two pylons is 5.1 m and the spacing between them is 5. The preliminary technical drawings that were used in this study assume a the total width of the trapezoidal deck of 10.4 m and a height of 2.3 m. For the reinforcing details and additional information related to the RC bridge's geometry refer to [60].

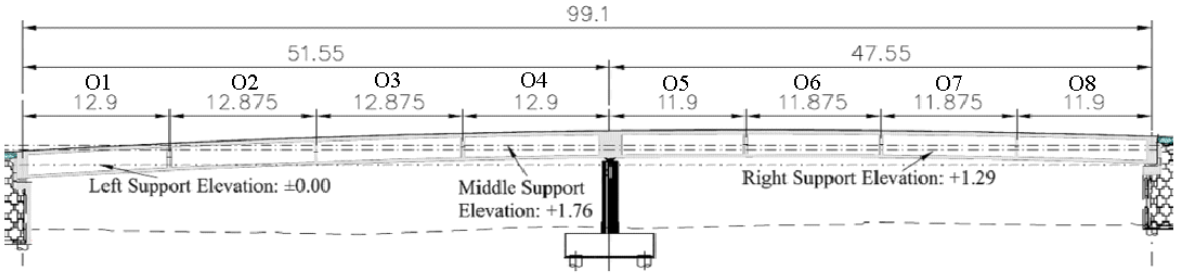

Figure 1. View of elevations.

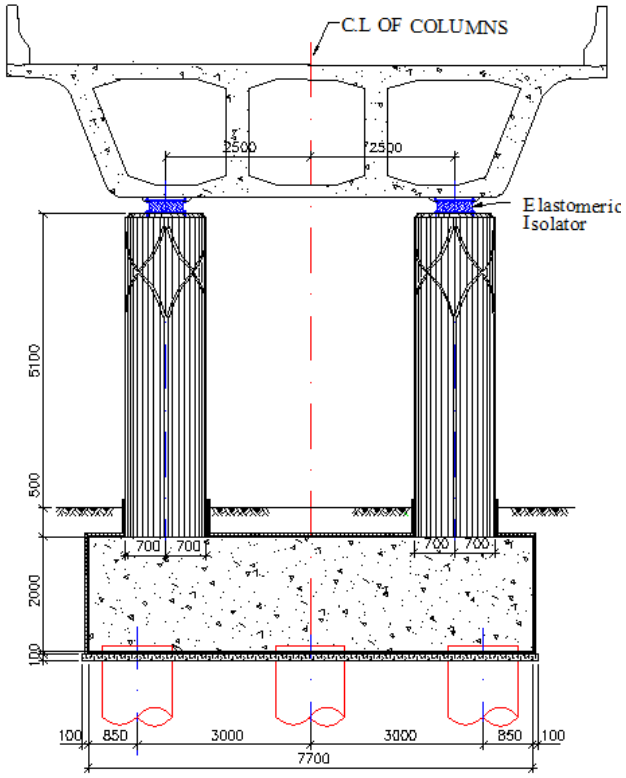

Figure 2. Geometry of the Pylons (dimensions in mm).

3 NUMERICAL IMPLEMETATION

3.1 Finite Element Mesh, Material and Load Assumptions

The under study RC bridge was discretized through the use of hexahedral elements as it can be seen in Fig. 3. In order to reassure a stable thus accurate finite element mesh, a convergence analysis was performed for different structural parts of the bridge, while the average

hexahedral element mesh size used in the construction of the FE mesh was 20 cm. The selected hexahedral element size was found to be optimum when using the Kotsovos and Pavlovic [51] material model, which is adopted in this work. For the case of the steel embedded rebars (Fig. 4) the Menegotto-Pinto material model was used. The total number of concrete hexahedral elements used in the FE mesh shown in Fig. 3 was 102,622 and the total number of embedded rebar macro-elements was 47,839 (Fig. 4). In Fig. 5 the detailed FE mesh is illustrated where the model of the 3D geometry of the connection between the deck and the two piers can be also seen. As it was presented in [60], after the completion of the mesh generation method, the total number of embedded rebar elements was 520,624 and the required computational time was approximately 43 minutes. The embedded rebar mesh generation procedure that was used to allocate and generate the embedded rebar elements was proposed by Markou [61], which was an extension of the Markou and Papadrakakis [62] work.

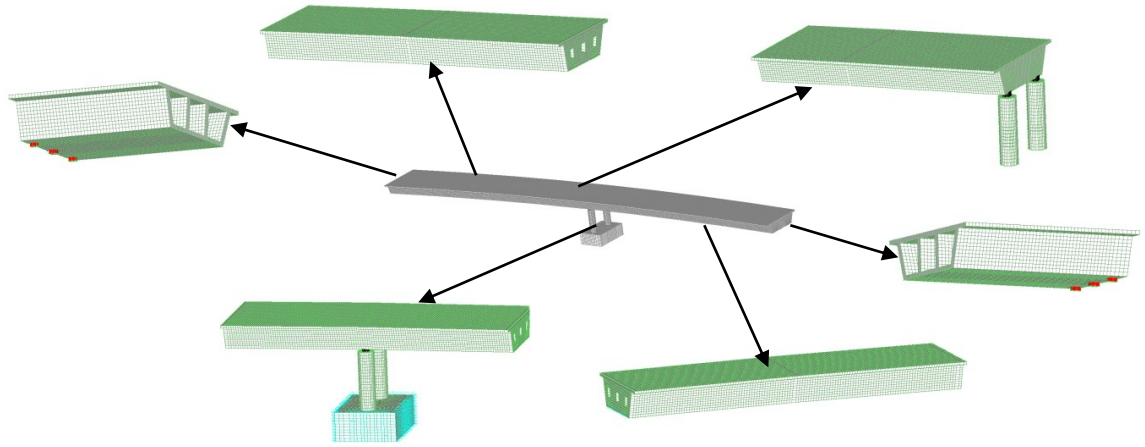

Figure 3. Models used for the mesh convergence analysis procedure.

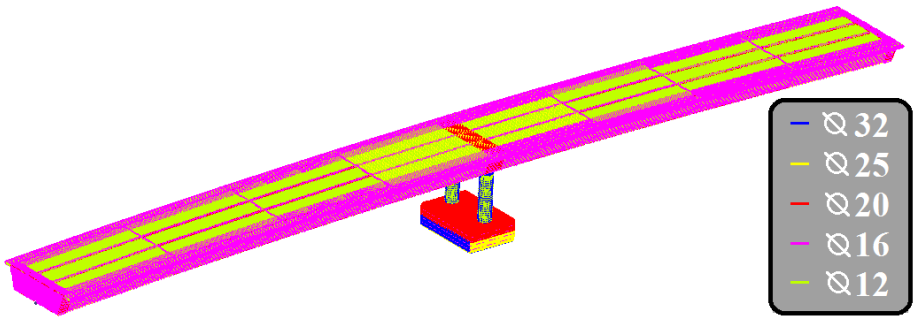

Figure 4. Macro-element rebar mesh.

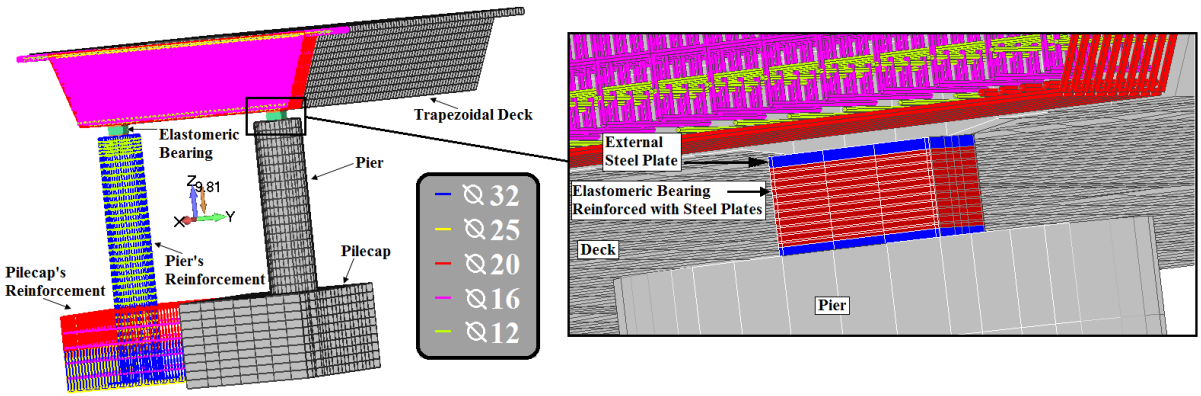

Figure 5. Detailed FE mesh of the bridge.

Table 1 shows the details related to the mesh used to discretize the RC bridge and the resulted embedded rebar elements. It is important to note here that the numerical data and results in Table 1 refer to the updated FE mesh that is used in this research work, which assumes a detailed modeling of the bearings through the use of 5,520 hexahedral elements (Fig. 6) instead of 312 that are used in [60]. The total number of bearings assumed is 8; three at the right and three at the left abutments, and two at the piers. Previous research work on 3D detailed modeling of standard reinforced elastomeric bearings can be found in [64].

a/a	Description	Value
1	Number of Hexahedral Concrete Elements	102,622
2	Number of Hexahedral Elements (Bearings)	5,520
2	Number of Nodes (hexa8 only)	175,784
3	Number of Macro-Elements	47,839
4	Total Number of Embedded Rebar FEs Generated	520,624
5	Total Number of Short Embedded Rebar FEs that were Discarded by the Filter Algorithm	1,439
6	Required Embedded Mesh Generation Time	42 m 22 s

Table 1. RC Bridge. General numerical details that derived after the solution of the complete FE model.

Due to the lack of data related to the materials of concrete and steel reinforcement, it is assumed that concrete is a C90 material and steel reinforcement an S500 material. Given that the bridge will be constructed in the UAE, the assumption of using a high strength concrete is common practice. The material properties that were adopted in the numerical models used are given in Table 2.

a/a	Material	Nominal Weight γ (kN/m^3)	Young Modulus E (GPa)	Hardening Ratio E_T (GPa)	Yielding Stress f_y (MPa)	Ultimate Stress f_u (MPa)	Ultimate Strain ε_u	Poisson Ratio ν
1	Concrete	24	44	-	-	90	-	0.2
2	Reinforcement Steel	78	200	2	500	695	0.10	0.3
3	Steel Plates	78	200	2	400	595	0.10	0.3
4	Elastomer	-	3,5 x 10^{-3}	-	-	30	-	0.49

Table 2. Material properties.

Fig. 7 shows the simplified FE mesh that was constructed in SAP2000, which discretizes the deck with 11,792 shell elements and the piers through the use of beam-column FEs. The reinforced elastomeric bearings are modeled through the use of two joint links. The compressive, shear and rotational stiffness coefficients (K_C, K_S, $K_{\theta X}$, $K_{\theta Y}$, $K_{\theta Z}$, see Eqs. 1-7) of each standard reinforced elastomeric bearing were computed according to [66] by using the material properties depicted in Table 2 that were found in [65] and the geometrical characteristics given in Fig. 6.

$$K_C = \frac{EA}{t_{rl}} \tag{1}$$

$$K_S = \frac{GA}{t_{rl}} \tag{2}$$

$$K_{\theta i} = \frac{EI_i}{t_{rl}}, i = X, Y \; and \; Z \; axis \tag{3}$$

$$E = E_b + \left[\frac{C_1 GS^2}{1 + \frac{C_1 GS^2}{0.75\,B}}\right] \tag{4}$$

$$E_b = 4G\left[1 - \left(\frac{q}{1+q^2}\right)^2\right] \quad (5)$$

$$q = {}^{L}/_{W}\,,\ L \text{ and } W\text{: length and width of the bearing } (W \le L) \quad (6)$$

$$C_1 = 4 + q(6 - 3.3q) \quad (7)$$

where E is the effective Young modulus, A the gross area of the elastomer, t_{rl} the total thickness of the elastomeric material, G the shear modulus (1 MPa within the range proposed in [2]), I_i second moment of inertia about axis i, q the ratio, C_1 the constant related to the shape of the bearing and B the bulk modulus (2 GPa [66]). The numerical results that derived after implementing the above equations for the case of the middle elastomeric bearing (connects the pier with the deck) can be seen in Fig. 7 (the formulas were programmed in Matlab).

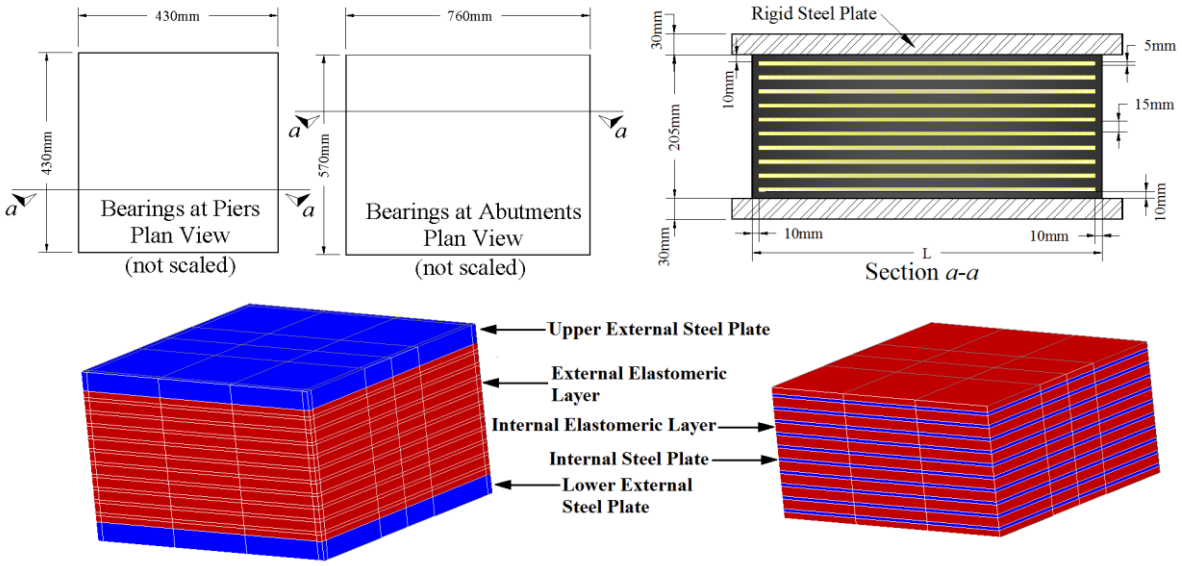

Figure 6. (Up) Geometrical features of the internal layers of the 8 elastomeric bearings and their plan views. (Down) Detailed FE mesh of the elastomeric bearings located at the heads of the two RC piers.

```
Shape Factor S                : 7.1667 unitless
Homogenous modulus Eb         : 3 MPa
Effective modulus E           : 282.9055 MPa
Compressive Stiffness Kc      : 337.4789 MN/m
Shear Stiffness Ks            : 1.1929 MN/m
Rotational Stiffness Kthetax  : 5.2 MNm/m
Rotational Stiffness Kthetay  : 5.2 MNm/m
Rotational Stiffness Kthetaz  : 10.4 MNm/m
```

Figure 7. Numerical data related to the middle bearings as they resulted from Eqs 1-7 [66].

In order to assess the mechanical behavior of the RC bridge preliminary design the following procedure was implemented: a. The elastomeric bearings were modeled separately through the use of 3D detailed numerical model and were assessed so as to determine their maximum carrying capacity (Fig. 6) b. The complete FE mesh of the bridge was solved through the use of both ReConAn and SAP2000 so as to derive the mechanical response of the bridge by assuming an elastic behavior for all material models and by applying only the self-weight of the structure. c. The complete 3D detailed model with embedded rebar elements was solved for the self-weight of the structure so as to determine the numerical response thus assess the mechanical behavior of the preliminary design of the structure. d. The 3D detailed model is used to perform nonlinear limit state analysis to determine the seismic

carrying capacity of the RC bridge after redesigning. The numerical findings of the above steps will be presented below.

3.2 Steel Reinforced Elastomeric Bearings

All elastomeric bearings were discretized by using both 8-noded (Hexa8) and 20-noded (Hexa20) hexahedral elements (see mesh for middle bearing in Fig. 8). The scope of performing this numerical investigation was to determine the carrying capacity of the bearings' initial design while parametrically investigate the mechanical behavior of the composite material of the reinforced elastomeric bearings under compression and shear loading. Newhouse et al. [63] performed 3D detailed analysis by using a hyper-elastic material model for the elastomer, so as to determine the deformation that occurs when bearings are positioned with a superelevation through the use of ANSYS [43]. As it was mentioned in their work, the numerical results were in a good comparison with the experimental data while they concluded that analysis through the use of solid FEs can be an effective research tool.

For the case of the two middle bearings that connect the piers with the deck of the at hand RC bridge, when assuming a 30 MPa ultimate stress their ultimate carrying load is 555 tons. This ultimate value is larger than the 300 tons proposed by the producer VSL [67], which is the ultimate load of a similar elastomeric bearing (400x500mm). According to the VSL specifications, by applying a load of 300 tons the bearing develops a 150 kg/cm^2. Accounting for the fact that the ultimate stress is 300 kg/cm^2 (30 MPa) then the required vertical load so as for the elastomer to reach the ultimate stress will be approximately double (600 tons). Therefore, numerically the model will fail when the rubber material reaches its maximum stress thus mechanically the elastomer will not be able to carry additional loads.

In this work, in order to simplify the analysis in terms of material complexity and computational demand, a typical von Mises material model is used to simulate the mechanical behavior of the elastomer and the steel plates. For this reason a numerical investigation was performed to determine the appropriate Young modulus of elasticity of the elastomer so as to derive realistic deformations according to the applied load. In addition to that, it is well known that for static loads the strain field within the bearing volume is mainly compressive in nature [63], with exceptions of tensile areas near the external elastomeric layers of the bearing (assuming that only a vertical load is implemented), thus the above assumption will not result significant differences. After performing the parametric investigation, which foresees the comparison between link elements (springs with stiffnesses equal to those given in Fig. 7) and the 3D detailed proposed model, it was found that when the elastomer is assigned a Young modulus of elasticity equal to 12 MPa, the two models derive similar results.

After the completion of the above parametric investigation, several analyses were performed in order to further study the numerical behavior of the model (for the middle bearings), which were mainly divided into two main categories. The first assumes that the load applied on the top steel plate of the bearing is a vertical load of 600 tons (so as to derive the ultimate carrying load V_u) and the second assumes four combinations of 18.5% (100 tons), 29.6% (160 tons), 37% (200 tons) and 50% (270 tons) of the derived ultimate vertical load V_u and a H_u = 20 tons horizontal nonlinear load. All analyses were performed by using both hexa8 and hexa20 FEs.

Fig. 8 shows the deformed shape of the Hexa20 FE mesh where the resulted vertical deformation for a vertical load of 540 tons (30 MPa ultimate stress was developed in the elastomeric material) was found to be equal to 30.4 mm which is 22.3% larger than the 24.8 mm that derived when using the Hexa8 FE. This is attributed to the more flexible numerical formulation of the Hexa20. It is evident that the elastomer expands vertically due to the excessive compression that is implemented at the external steel plate, where the laminated steel

plates constrain this lateral expansion. As Fig. 8 shows, the elastomer material at the external layer expands laterally due to the compression thus a folding type of deformation develops due to the steel plate reinforcement. A similar type of folding is noted in Fig. 9 in a real bearing specimen tested by Newhouse et al. [63] where the loading type was a combination of compression and horizontal load that derived from the pad's superelevation.

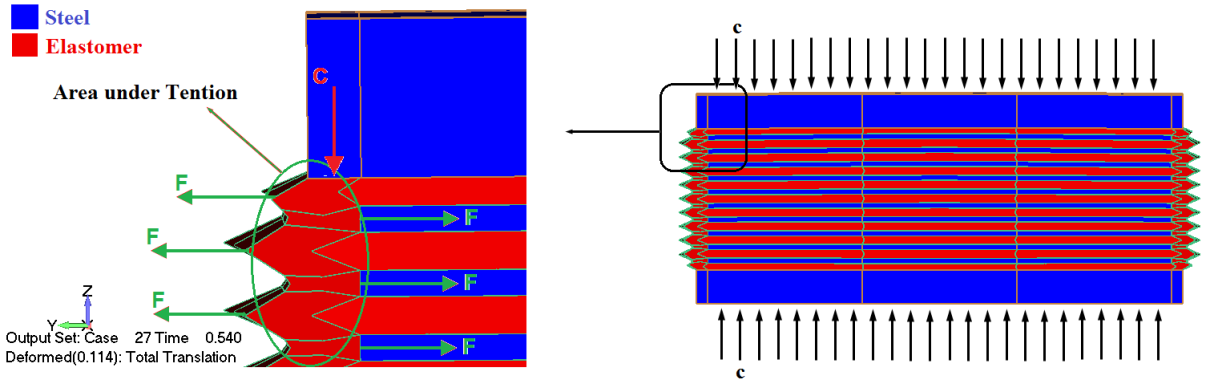

Figure 8. Hexa20 model. Deformed shape for V = 540 tons or 5.4MN.

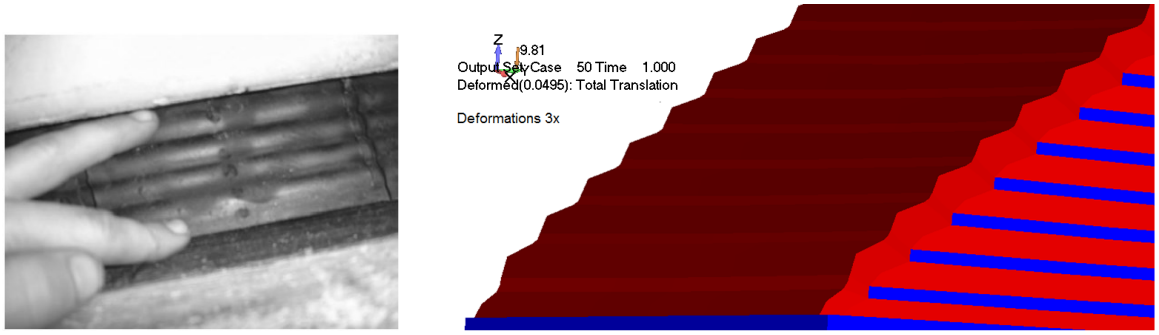

Figure 9. (Left) Deformed shape after tension debonding of reinforced elastomeric bearing with steel plates [63] and (Right) Deformed shape of bearing as it resulted from the Hexa20 model (50% V_u + 100% H_u).

Load Combination	Linear Vertical Dead Load V (tons / a%V_u)	Max. Vertical Displ. at the 1st load step (mm)		*H* Load for which zz-tension occurs at the elastomeric layer at the base (tons)		Maximum Horizontal Displ. for (mm)		Max. vertical expansion of the elastomeric layer at the base (mm)	
		Hexa8	Hexa20	Hexa8	Hexa20	Hexa8	Hexa20	Hexa8	Hexa20
1	100 / 18.5	4.87	5.71	28	44	45.6	46.8	0.15	0.22
2	160 / 29.6	7.76	9.11	44	68	46.1	47.6	0.1	0.16
3	200 / 37.0	9.70	11.4	56	84	46.6	48.2	0.07	0.13
4	270 / 50.0	13.1	15.3	72	112	47.5	49.5	0.04	0.08

Table 3. Numerical results as they derived from the analysis, when applying different load combinations.

After the completion of the first set of analyses (only vertical loads), the next set of numerical results derived by assuming different levels of vertical loads (which are assumed to be dead linear loads that are implemented at the first loading increment) and a horizontal load of 20 tons that was applied incrementally at the top external steel plate. The derived numerical results are summarized in Table 3. From the resulted numerical output, it can be concluded that the bearing's deformation is controlled mainly by the horizontal load given that its compressive stiffness is much larger than the corresponding shear. Fig. 10 shows the deformed shape and z-displacement contour of the Hexa20 model for the load combination 1. As it results, tension develops at the external elastomeric layer and the lower area of the bearing (1st elastomeric layer at the base and the bottom steel plate), which eventually tends to lift up.

Therefore, the larger the vertical load applied the smaller is the vertical lift up due to the horizontal loading.

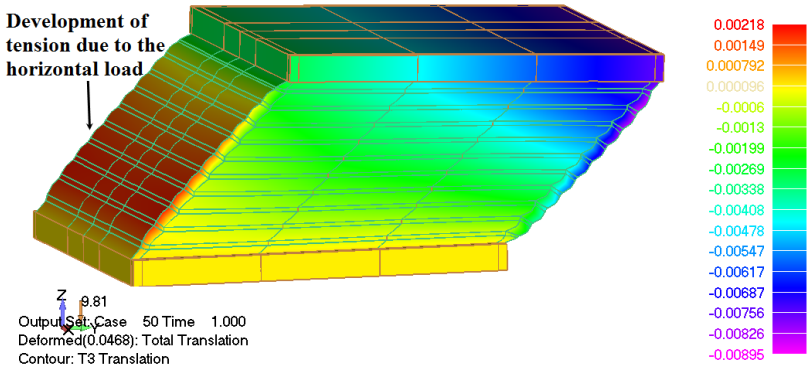

Figure 10. Deformed shape and translation contour along the z-axis of the elastomeric bearing due to the load combination 1 (Hexa20 FE model – Load Combination 1).

3.3 Linear Elastic Solution without Embedded Rebars

The next stage of assessing the numerical model and the overall mechanical behavior of the under study bridge was to linearly analyze the complete hexahedral model (Hexa8) by assuming only the self-weight of the structure. The results of this analysis were compared with the results that derived from the simplified SAP2000 FE model (Fig. 11) for which a mesh sensitivity analysis was performed in order to determine an optimum FE mesh size which will provide an acceptable accuracy and computational efficiency. Three FE sizes were tested (130 cm, 70 cm, 30 cm) and it was found that when discretizing the bridge by using rectangular FE shells with an edge size of 70 cm the numerical response of the mesh satisfied the above demands. Fig. 12 shows the z-axis translation contour as it derived from the Hexa8 FE mesh, where it results that the maximum deflection of the bridge is located at the left span of the deck and it is equal to 53.7 mm. The corresponding maximum deflection that resulted from the simplified model was 47 mm (Fig. 11) which is smaller. It was also found that the compressive deformation due to the bearings at the piers was 21 mm and 26.5 mm for the simplified and the detailed model, respectively. Therefore the difference in the maximum deflection results from the deformation of the elastomeric bearings. One of the reasons that the bearing's displacement for the case of the Hexa8 model is larger than the corresponding simplified model is the fact that ReConAn increases the nominal weight of concrete by 1.03 so as to account for the reinforcement self-weight. By representing the axial force that develops due to the self-weight of the structure at the top surface of each pier, according to SAP2000, the resulted compressive force equals to 5.83 MN. This level of compression exceeds the ultimate carrying capacity of the bearings (5.55 MN) that connect the piers to the deck thus redesigning will be required (increase of the bearings area). Fig. 13 shows the deformed shapes of the bearings at the middle and the abutments as they resulted from the Hexa8 model. It was found that the longitudinal x-translation of the left abutment was equal to 6.9 mm, while the simplified model derived a corresponding 3.1 mm. This finding confirms that the selected material properties for the case of the elastomer result a more flexible numerical behavior in comparison to the link element used in the simplified model.

It must be noted that the deflection differences, regarding the deck mechanical response, would have been larger if the shell FE mesh was enriched with kinematic constraints at the middle vertical diaphragm which has a total thickness of 2 m. This structural member induces additional stiffness in the deck's mechanical behavior thus when discretizing with shell FEs the actual stiffness contribution in the middle of the bridge cannot be captured realistically.

The same phenomenon applies for the 1 m thick vertical diaphragms located at the two ends of the bridge's trapezoidal deck.

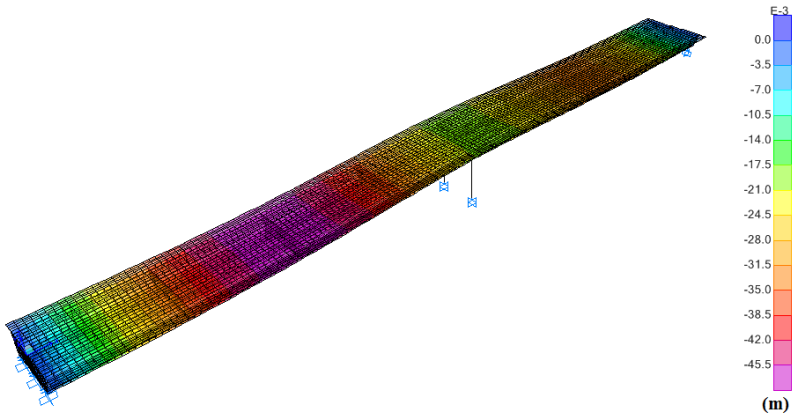

Figure 11. SAP2000 (Shell FEs). Deformed shape and translation contour along the z-axis of the RC bridge due to the self-weight.

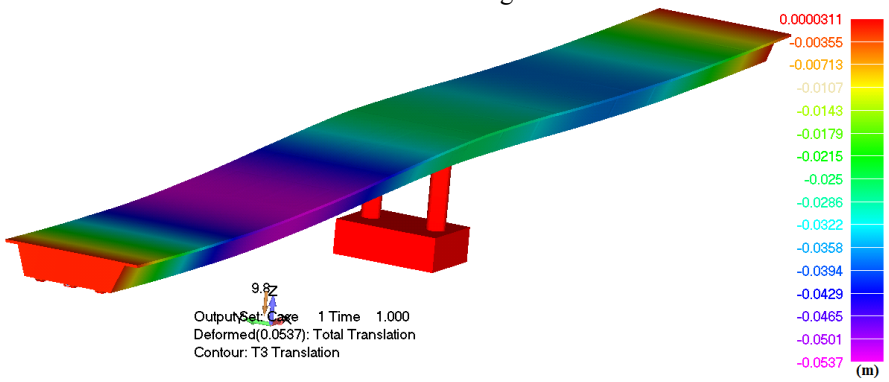

Figure 12. ReConAn (Hexa8 FEs). Deformed shape and translation contour along the z-axis of the RC bridge due to the self-weight.

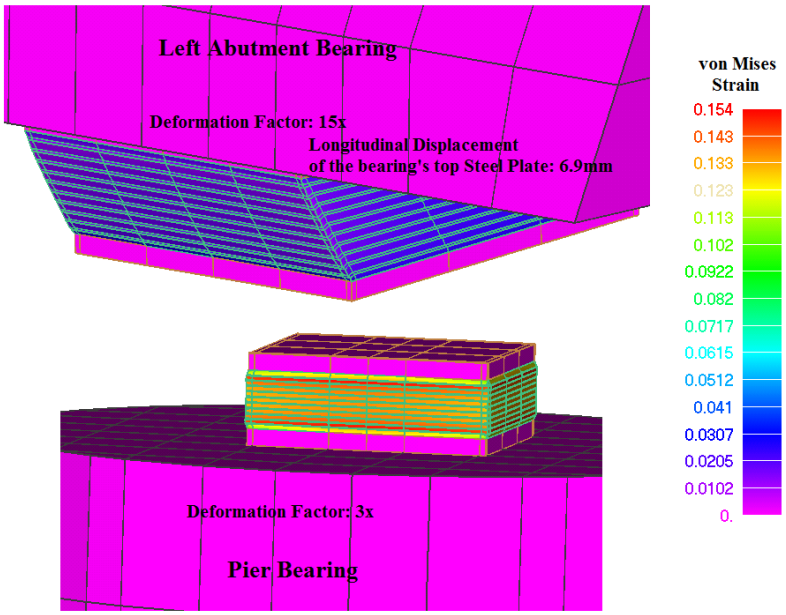

Figure 13. von Mises strain contour of the middle and left abutment elastomeric bearings.

An additional finding that resulted from this linear analysis is that the areas where the elastomeric bearings are connected with the deck develop stress concentrations, which are higher in the case of the simplified model due to the assumption that the bearings are modeled

through the use of link elements. The link elements are connected to the deck at a single node which contributes to this numerical phenomenon. Fig. 14 shows the solid von Mises stress contours for both models as they derived from the analysis. As it can be seen, the simplified model derives an 18.1 MPa von Mises stress at the connection areas of the bearing with the deck, while the 3D model results a 14.7 MPa von Mises stress. The deformed shape of the bearings can be seen in Fig. 13, where the solid von Mises strain contour is visualized.

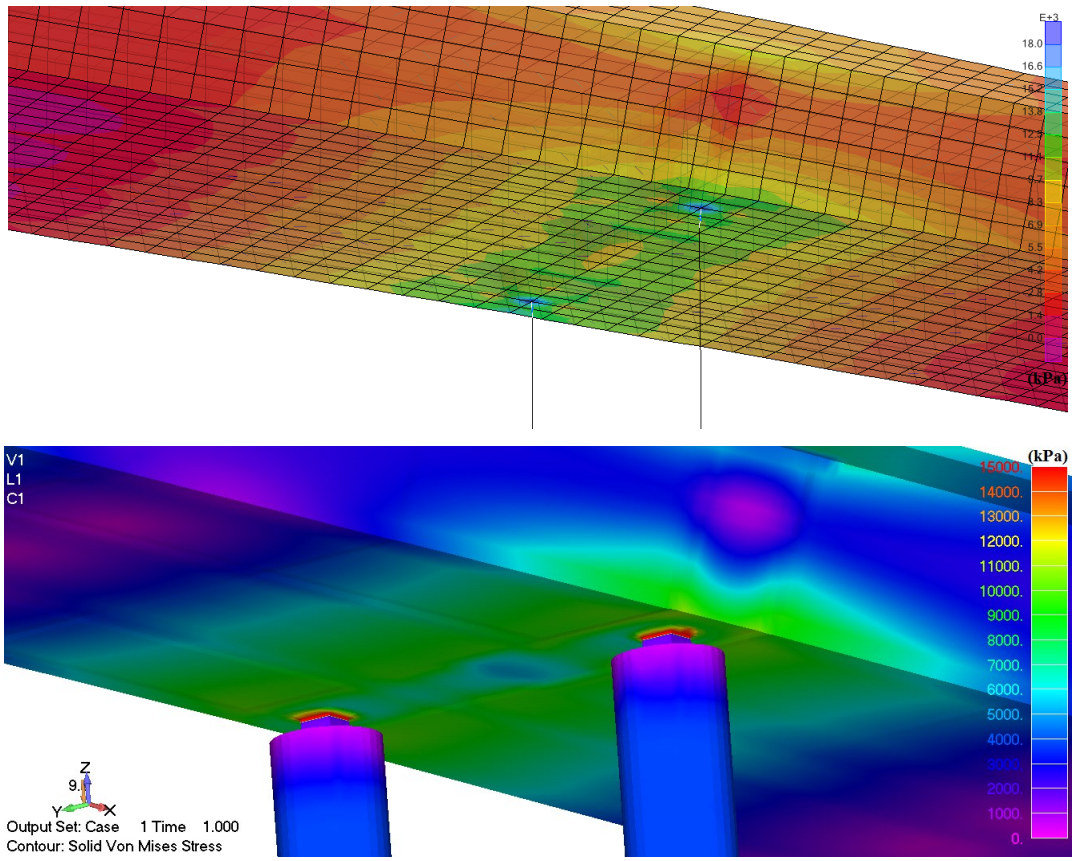

Figure 14. von Mises stress contours. (Up) Sap2000 and (Down) ReConAn.

The next assessment stage is to determine whether the RC bridge develops any cracks due to its self-weight thus the use of a pretension system will be required. The resulted maximum deflection from the linear analysis for the self-weight of the structure revealed that the behavior of the deck is relatively flexible given that pretension was not assumed.

3.4 Nonlinear Solution of the Complete 3D Detailed Model

In this section the numerical results that derived from the nonlinear solution of the complete 3D detailed model with embedded rebars will be presented. The FE mesh of Fig. 5 is used so as to simulate and investigate the mechanical behavior of the RC bridge under its self-weight. The aim of this numerical analysis is to investigate any stress concentrations and potential cracking development that eventually will reveal the weak areas of the bridge according to its preliminary design. The current model does not foresee any posttensioning thus cracks may develop.

After performing the analysis, the numerical results revealed that the RC bridge is not capable of carrying its self-weight without the development of cracks, therefore if we had assumed the service loads, the deck would have developed larger cracks. As it can be seen in Fig. 15, due to the relatively long spans of the bridge the lower area of the deck located at the

right span of the bridge develops horizontal cracks which are attributed to the stress field derived from bending and shear forces that are developed at the connection area between the vertical walls and the lower slab of the RC deck (Fig. 15c). At the left span of the bridge cracking was developed at the vertical diaphragm and at the middle area of the vertical walls (Figs. 15a and 15b, respectively).

Fig. 16 shows the von Mises stress contour that derived from the numerical analysis for the self-weight of the bridge at the pier's head, where the transfer of the compressive loads of the deck can be visualized. So as to represent the stress distribution that derives from the above procedure in a more revealing way, Fig. 16 shows the section cut of the model at the pier's bearing. The two bearings at the piers were found to be under designed (elastomeric material exceeded significantly the 50% of its ultimate stress) thus an increase of their plan view area was required.

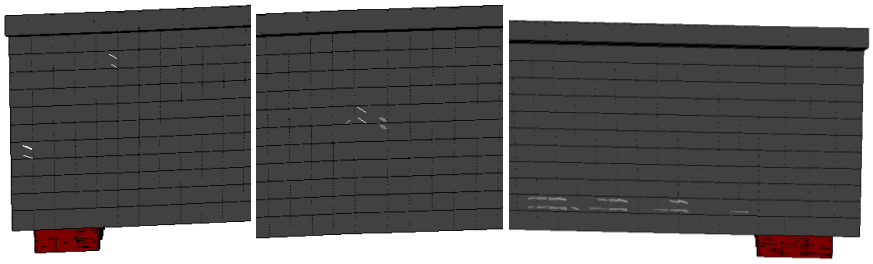

a. b. c.

Figure 15. Crack patterns of the deck due to the self-weight load at the a. left support, b. middle of the left span and c. near the right support.

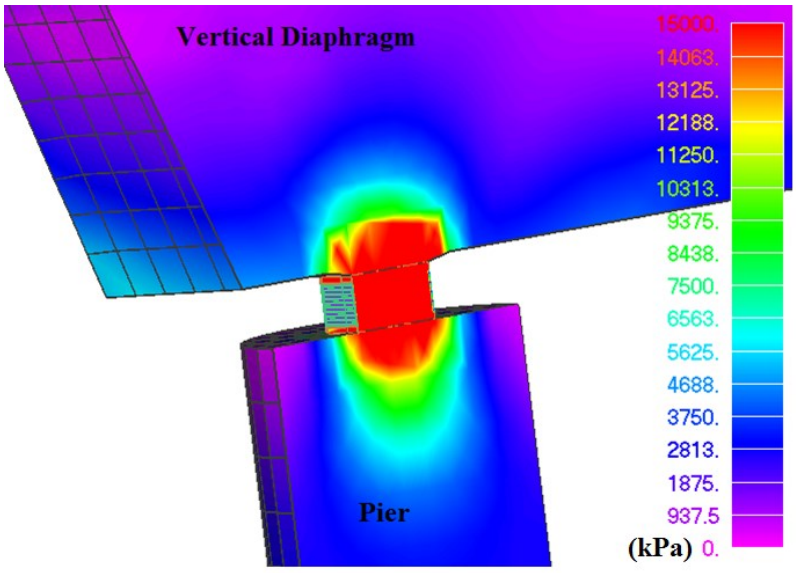

Figure 16. von Mises stress contour at the connection between the pier and the deck (section).

The maximum displacement of the bridge was found to be equal to 30.4 mm (middle nodes of the left span of the bridge). The stiffer behavior in comparison to the previous two models is attributed to the reinforcement that is modeled through the use of embedded rebar elements. It is evident that for this case, the reinforcement increases the stiffness of the deck in terms of the material behavior and the resulted maximum deflection was found to be decreased and smaller than both models that were presented in the previous section.

3.5 Redesign of the RC Bridge and Nonlinear Push Over Analysis

In this section the numerical results that were computed by using the modified FE mesh will be presented. As it was presented above, it was found that the bridge's mechanical response was not satisfactory for two main reasons: a. it develops relatively large deflections and b. cracks when the self-weight of the structure is applied. The relatively large deflections develop due to the soft behavior of the bearings located at the piers and the design of the deck's section. So as to alleviate these design issues, the elastomeric bearings at the piers were redesigned and their new dimensions are increased to 70x70cm, while the deck was reinforced with a posttensioning system which can be depicted in Fig. 17. The vertical walls are reinforced with three posttension cables that are modeled as embedded reinforcement with prestressing properties.

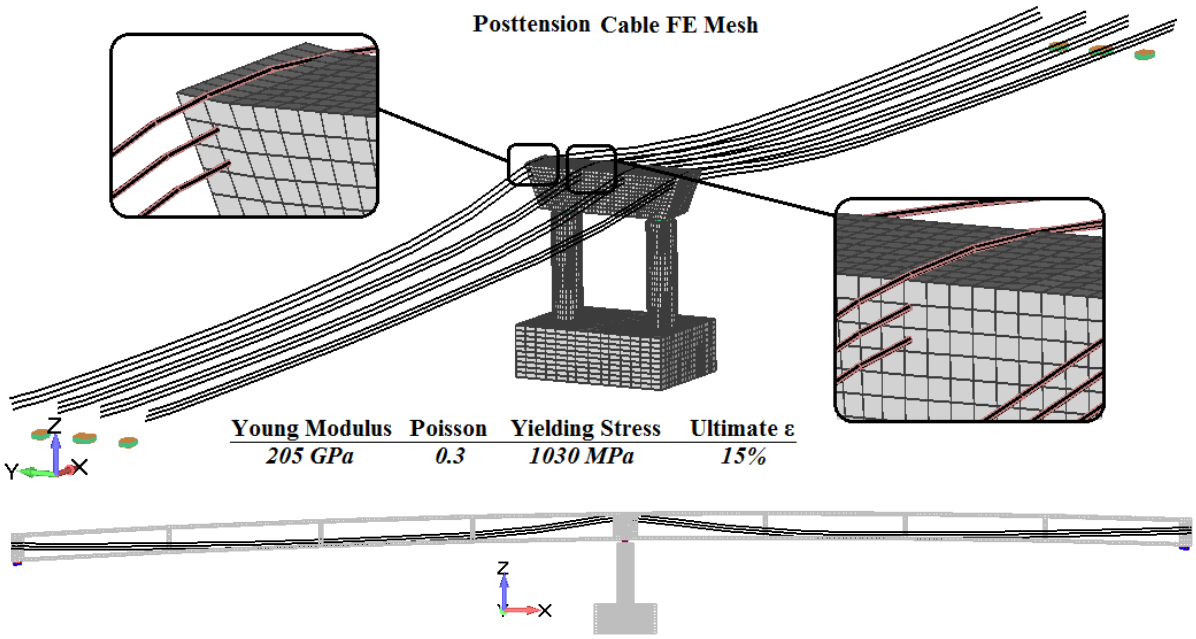

Figure 17. Material properties and FE Mesh of the posttensioned cables.

BEAM Property 11 - PrestressFi90_5MN

SMAD custom properties

Reinforcement property

Property	Value
Slip Flag (0:NoSlip)	0
Type of Element for Reinf. 1:Rod 2:NBCFB(rect.) 3:NBCFB(circ.)	1
Number of Fibers (if NBCFB)	0
Number of Integ Points (if NBCFB)	0
Material Flag (1:Bilinear 2:Menegotto Pinto)	1
Flag (always 1.0)	1
Steel Young Modulus	205000000
Steel Poisson	0.3
Steel Hardening	2050000
Steel Fy	1030000
Steel Failure (ef = 0.12)	0.15
Prestressed (0:No 1:Yes)	1
Prestressed Force (kN)	5000

Figure 18. Define posttensioning force for an embedded rebar property.

It is generally accepted that pre- and post- tensioning can be modeled by applying temperature change or a set of axial and distributed loads [42] on the RC structural member which is under compression (due to the pre- or post- tensioning). For the needs of this research work, ReConAn was integrated with the numerical ability of accounting pre- and post- tensioning forces applied directly at the cables that are modeled as embedded rebar elements. Fig. 18 shows the SMAD Custom Properties software developed by Stavroulakis [68], through which the pre- or post- tension force is defined as a custom property.

The algorithm that was developed so as to account the compression induced to concrete hexahedral elements at the material level, foresees the calculation of the initial stress σ_{i0} and ε_{i0} strain developed internally in the embedded posttensioned cable by using Eq. 8, while the internal force of the embedded cable $\boldsymbol{F}_{R,Int.}$ is transformed through the use of the kinematic expression given in Eq. 9, into a hexahedral internal force matrix $\boldsymbol{F}_{H,Int.}$ that is defined as the initial force condition of the hexahedral element. Then the internal force matrix of the hexahedral element that incorporates the corresponding embedded cable element is converted into an external load matrix $\boldsymbol{F}_{H,Ext.}$ through the use of Eq. 10, and applied to the corresponding hexahedral nodes. The numerical implementation of the posttensioning effect takes place in the first load increment where the computation of the initial stress state of the numerical model takes place. After the completion of the first load increment the nonlinear load is applied incrementally until complete failure, while the new stresses and strains are computed according to Eq. 11.

$$\sigma_{i0} = \frac{F_P}{A_i} \quad \varepsilon_{i0} = \frac{\sigma_{i0}}{E_S} \tag{8}$$

$$\underbrace{\boldsymbol{F}_{H,Int.}}_{(24x1)} = \underbrace{\boldsymbol{T}}_{(24x6)} \cdot \underbrace{\boldsymbol{L}}_{(6x2)} \cdot \underbrace{\boldsymbol{F}_{R,Int.}}_{(2x1)} \tag{9}$$

$$\underbrace{\boldsymbol{F}_{H,Ext.}}_{(24x1)} = - \underbrace{\boldsymbol{F}_{H,Int.}}_{(24x1)} \tag{10}$$

$$\sigma_{i+1} = \sigma_{i0} + \Delta\,\sigma_{i+1} \quad \varepsilon_{i+1} = \varepsilon_{i0} + \Delta\,\varepsilon_{i+1} \tag{11}$$

A parametric investigation was performed in order to verify the numerical performance of the proposed algorithm which explicitly models the posttensioning system. Fig. 19 shows two of the FE models that were developed in order to investigate the developed algorithm. The two RC beams foresee two different cable geometries through which the posttensioning force will be applied to the RC beams. Both models have 2 cables of 28 mm in diameter, while the first model assumes a straight cable placed at a 63 mm distance from the lower cord of the beam and the second model uses a curved cable geometry. The total applied posttensioning force was 100 kN per cable which was set so as to avoid any cracking in the concrete given that the beams are assumed to be weightless in an attempt to investigate the mechanical behavior induced from the posttensioning cable. The cable's yielding stress was equal to 555 MPa thus the 100 kN force represents only a 30% of the yielding force of the cable. The concrete's uniaxial compressive strength was set to 22.5 MPa.

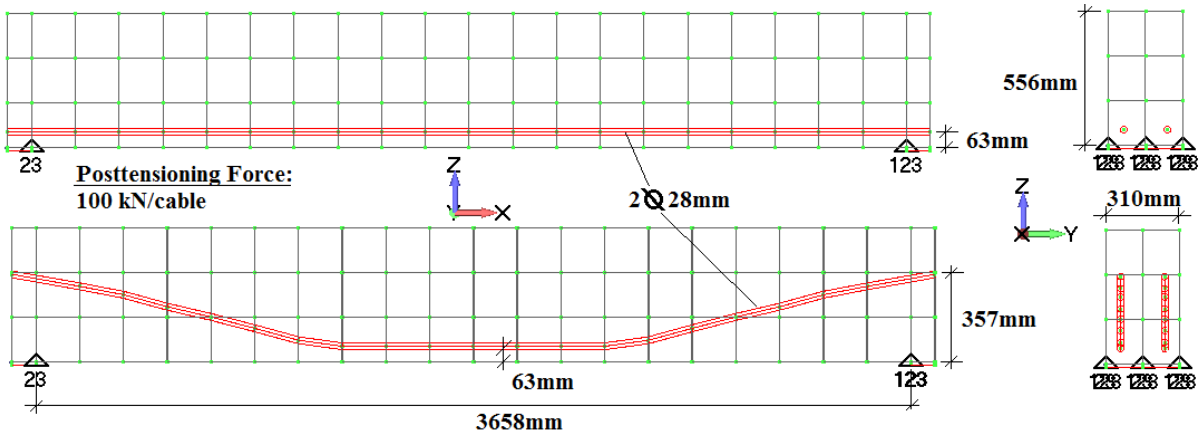

Figure 19. RC beam models with straight and curved posttensioning cables.

After analyzing the two models the derived uplifting maximum displacements were equal to 0.483 mm and 0.45 mm, for the first and second model, respectively. Fig. 20 illustrates the

deformed shapes of the two models and the XX stress contours as they resulted from the analysis. As it can be seen the contour levels that are used in both models are the same so as to compare the resulted stress fields in terms of compression and tension that results along the longitudinal axis of the beam. It is obvious that the posttensioned cable generates a compressive stress field at the lower level of the beam in both cases, while a tension is developed at the top cord of the two beams. In addition to that, the second model has a part of the top cord under tension (approximately 60% of the top cord is under tension) while the rest of the upper cord is under compression along the longitudinal axis of the beam. This is attributed to the curved geometry of the cable, which foresees the two ends of the cable to be located above the centroid of the two end sections located at the supports (see Fig. 19). Fig. 21 shows the deformed shape of the second model when the self-weight of the beam is accounted for.

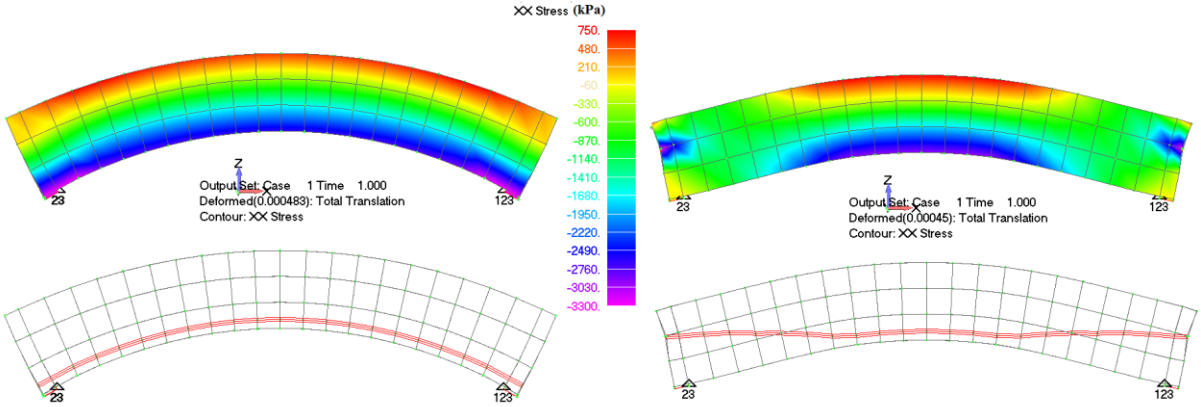

Figure 20. XX stress contour and deformed shape of the two RC beam models due to the posttensioning force (self-weight of the beam is neglected in both FE models).

An ultimate limit state analysis was performed for the case of the second model by applying a uniform distributed load on the top cord of the beam's section. Fig. 22 shows the resulted P-δ curve as it derived from the numerical analysis. As it can be seen, the beam has a negative displacement (uplift due to posttension) until the total vertical applied load reaches the 80 kN of magnitude. The P-δ curve shows that the first cracking occurs for a total load of 213.2 kN and that the beam fails for a total load of 754.5 kN and a 15.2 mm maximum deflection. The same RC beam was analyzed but without assuming any posttensioning (see P-δ curve in Fig. 22), so as to compare the mechanical behaviors of the same beam geometries and reinforcement, where one beam was prestressed and the other was not. The beam without posttension, cracks from the first load increment, while it fails for a smaller load. Fig. 23 shows the deformed shapes and the crack patterns for characteristic load levels as they resulted from the analysis of the beam with posttension.

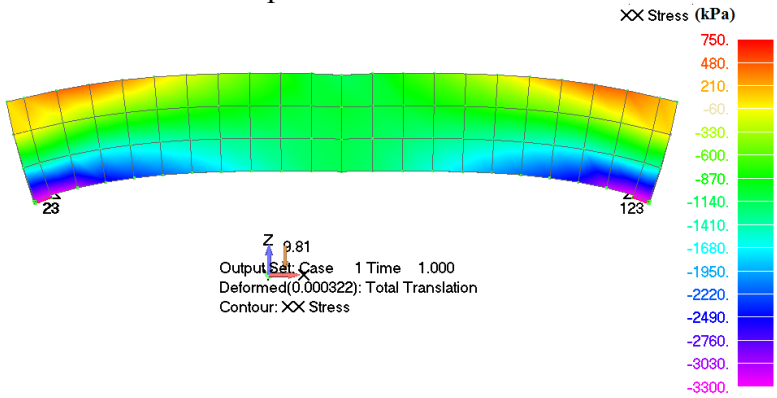

Figure 21. XX stress contour and deformed shape of the RC beam model with the curved cable (self-weight of the beam is accounted for).

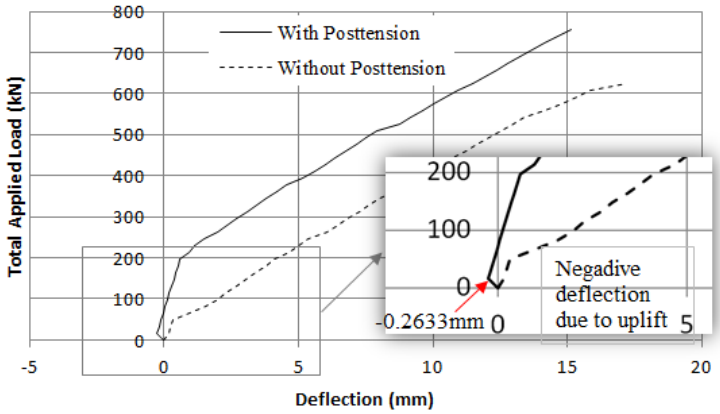

Figure 22. P-δ curve for the case of the second model (curved cable with posttension).

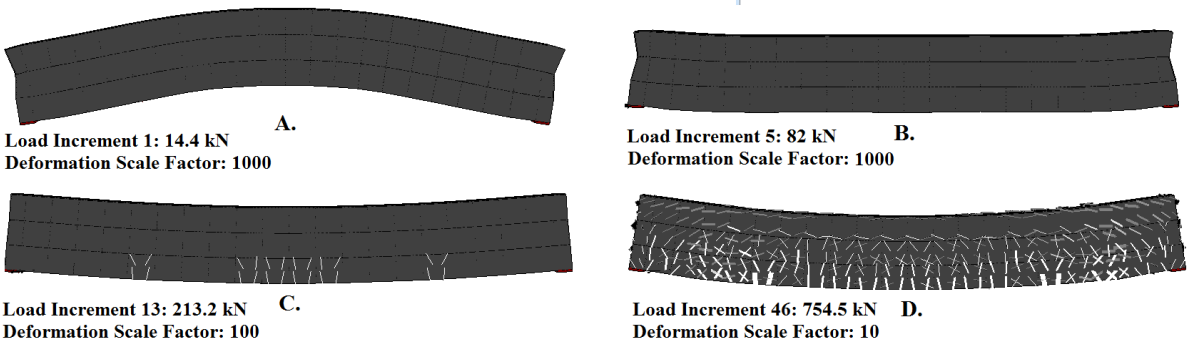

Figure 23. Deformed shapes and crack patterns for the case of the second model (curved cable with posttension).

After the parametric investigation of the posttensioning algorithm the numerical model of the RC bridge was solved by neglecting the self-weight and any other gravitational loads so as to investigate the overall behavior of the bridge due to the posttension. It is important to note that each cable element is assumed to have a circular section of 90 mm in diameter, while for this first full-scale posttensioning analysis it was assumed that the applied prestress force was equal to 250 kN (5% of the final applied prestress force).

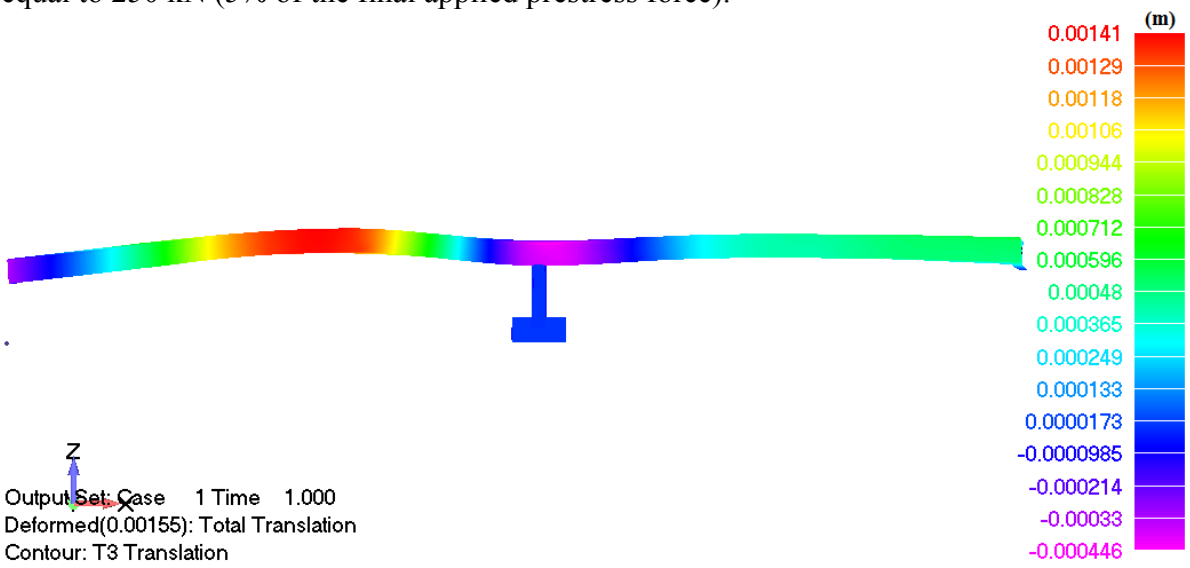

Figure 24. Deformed shape of the RC bridge due to posttensioning (self-weight is not accounted).

Fig. 24 shows the resulted deformed shape due to the prestress force applied in the 12 post-tensioned cables embedded in the four vertical walls of the RC deck. As it can be seen the two spans uplift while the middle elastomeric bearing is under compression due to the negative

moment developed at the area where the deck connects with the piers (posttensioned cables have a negative eccentricity, see Fig. 17). This numerical finding points out that the posttensioning system results an additional vertical load that is transferred to the bearings connecting the piers with the deck. The same observation was made by applying the prestress in the simplified model in SAP2000 by assigning negative strain at the shell elements of the deck that incorporate the prestress cables.

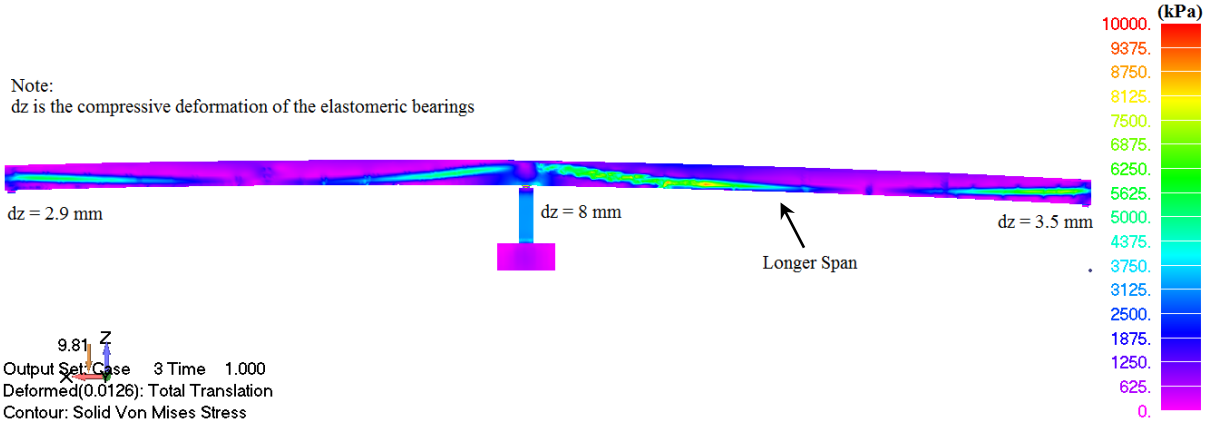

Figure 25. Deformed shape and von Mises stress distribution for service loads.

Given that the purpose of this work is to assess the seismic capacity of the bridge, presenting the posttensioning system's assessment will not take place below. It is important to note that the final model used to perform the push over analysis assumes a prestress force of P_p = 5000 kN per cable. Fig. 25 shows the von Mises stress distribution of the bridge as it resulted from the analysis by assuming the service loads (self-weight of the bridge, self-weight of the asphalt layer and the live load). According to the analysis the maximum deflection (including body translation) of the longest span of the deck, was equal to 12.6 mm, its maximum deflection relative to the supports, was equal to 5.8 mm, while the corresponding compressive deformation of the elastomeric bearings at the piers was 8 mm (Fig. 25).

a/a	Parameter	Value
1	Ground Type	B
2	Soil Factor S	1.2
3	Importance Factor γ	1.3
4	Acceleration a_g	0.2g
5	Behavior Factor q	1.0
6	Limit of the constant spectral acceleration branch T_C	0.5 seconds
7	Mode along the Y-axis T	1.36 seconds
8	Design Spectrum Acceleration $S_d(T) = a_g S[2.5/q][T_C/T]$	0.191g
9	Total Base Shear V_S	7.66 MN

Table 4. Seismic parameters assumed for the computation of the total base shear according to EC8.

The final step before performing the push over analysis was to calculate the total quasi-static seismic load and apply it on the model. As it is described in [3], one of the most commonly used methods to perform nonlinear analysis for the derived seismic loads is the Modal Push over Analysis (MPA), which is the method adopted in this work. The total seismic load was calculated according to EC8 [1] by using the type I response spectrum. The assumptions made for the calculation of the design spectrum acceleration and total base shear are given in Table 4.

After performing the modal analysis through the use of SAP2000, it was found that the under study bridge has its two first modes being translational oscillations along the X and Y axes, respectively. Given that the Y axis is the lateral axis of the model, the push over analysis was performed by applying the horizontal seismic load on the deck's vertical wall along the Y global axis (2nd dominant mode, see Fig. 26).

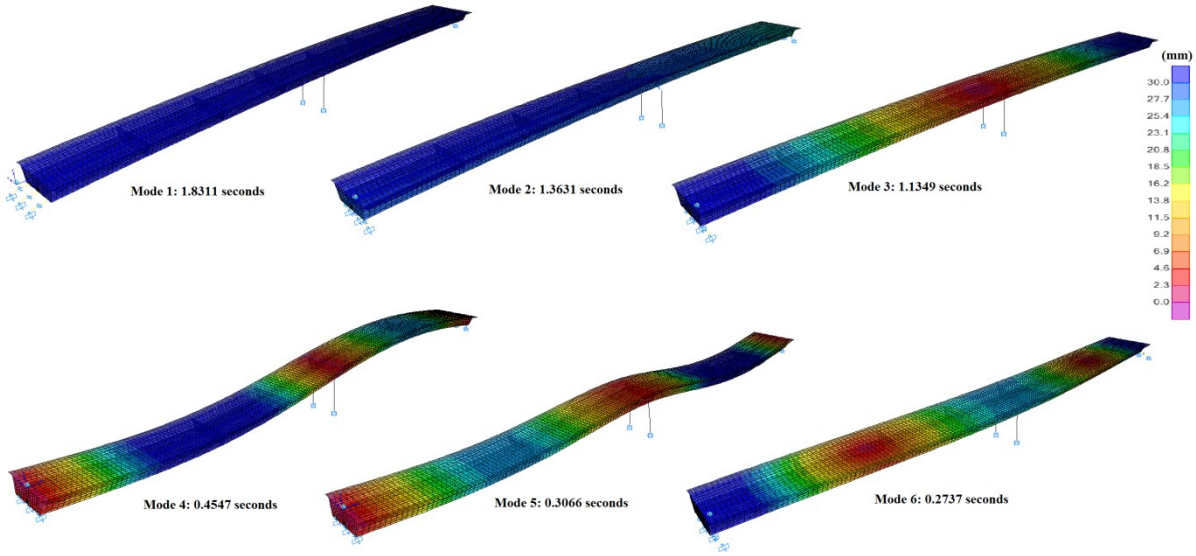

Figure 26. Mode shapes as they derived from SAP2000 (simplified model).

A total of 15MN were applied on the vertical wall of the deck through the use of 10 load increments. The work convergence criterion was set equal to 10^{-4} while it is relaxed to a 10^{-3} in the case that the required internal iterations were more than 10, in an attempt to decrease the computational time and retain an acceptable numerical accuracy. It is important to note here that when solving a hexahedral mesh with more than 100,000 elements the numerical errors that are generated due to the accuracy of the calculations used in the algorithm alone, are significant given the large number of elements, thus using a numerically unstable material model that releases significant unbalanced forces during each iteration especially when cracking occurs, achieving convergence becomes a numerically cumbersome task. The corresponding derived errors for the under study model are shown in Fig. 27.

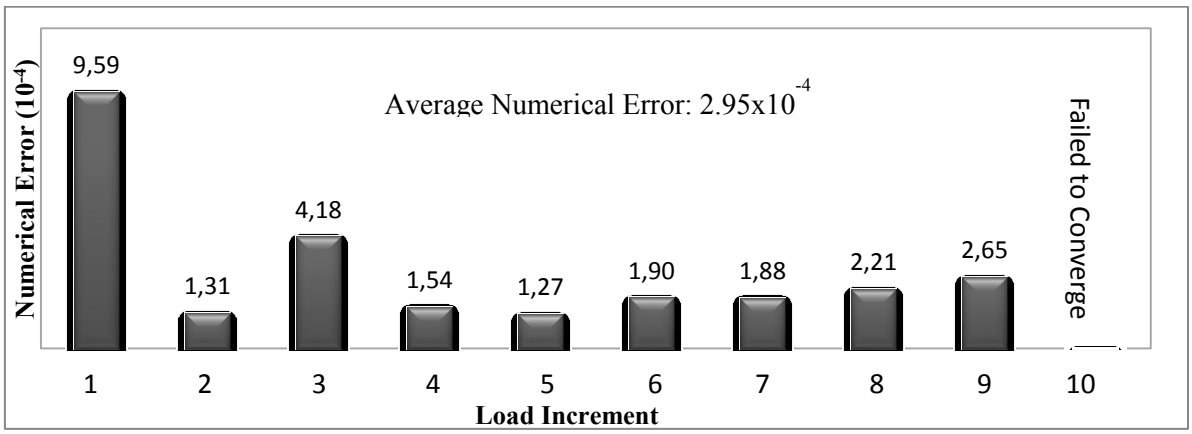

Figure 27. Numerical errors per load increment as they resulted from the nonlinear analysis.

The numerical results from the nonlinear analysis showed that the deformed shape of the under study bridge due to the horizontal load was similar to the 2nd modal shape while the elastomeric bearings were the structural members that developed significant deformations. As

it can be seen in Fig. 28, point β which is located at a distance of 39 m from point α, exhibits the maximum horizontal displacement, while the deck behaves as a beam under bending. In addition to that, the left span (which is the longest one) transfers a larger load to its left support (point α) and this is the reason why the horizontal displacement of the deck at the left support is larger than that of the right support (point δ). Fig. 29 shows the resulted P-δ curves for the four monitored points (α, β, γ & δ) shown in Fig. 28 and the corresponding curves of the top nodes of the two piers. As it can be observed from Fig. 29, the two piers do not exhibit the same horizontal displacement given the rotation of the deck about the Z global axis (Fig. 30), thus the overall deformation of the bridge was asymmetric.

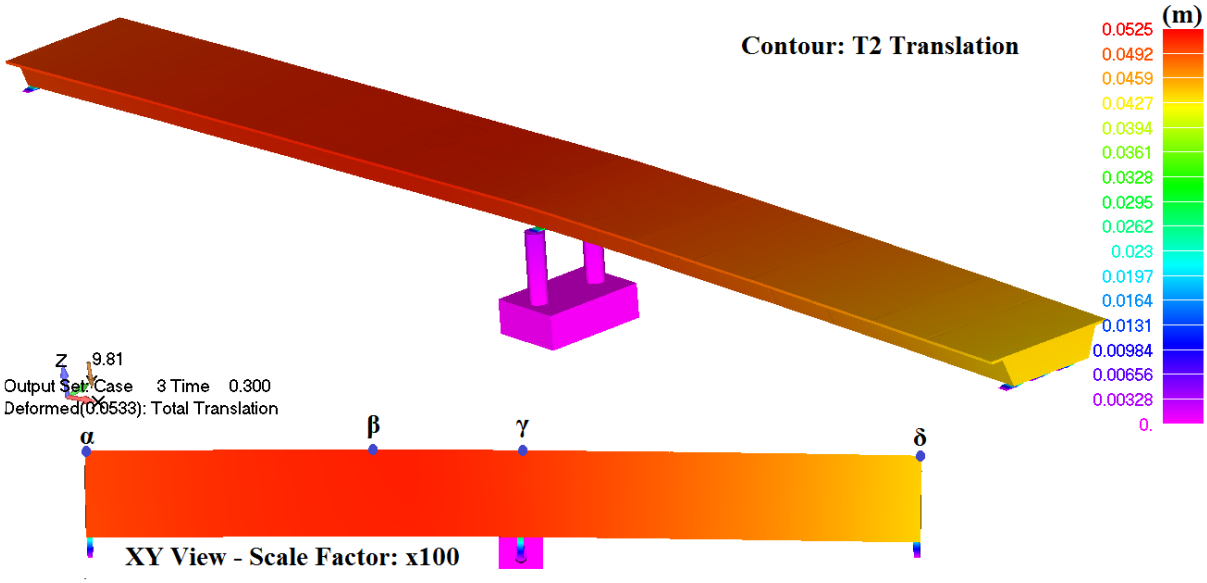

Figure 28. Deformed shape at load increment 3 (Total applied horizontal load 4.5 MN).

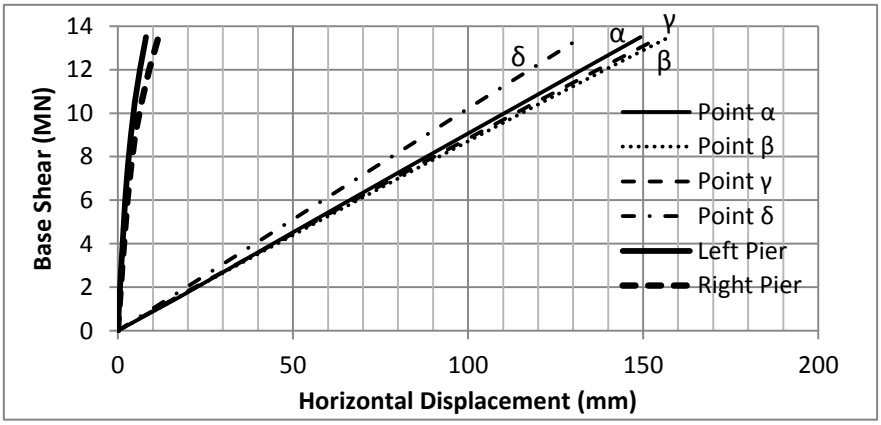

Figure 29. P-δ curves.

It is evident that the failure mechanism is controlled by the elastomeric bearing while the deck of the bridge does not develop any significant cracks prior to complete failure (V_{max} = 13.5 MN). The final model of the RC bridge is capable of carrying the code's design base shear demand (7.66 MN) and the piers manage to resist to the developed bending moments at their base. The maximum horizontal displacement prior to failure was found to be equal to 157.4 mm which is attributed to the use of elastomeric bearings that decouple the mechanical behavior of the deck and the piers thus modify significantly the stiffness of the bridge. It is evident that the piers and the deck does not deform significantly so as to develop rebar failures or even in this case rebar yielding.

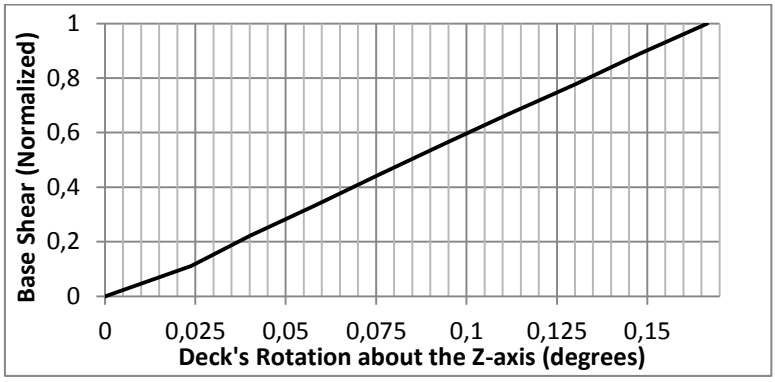

Figure 30. Deck's rotation due to the horizontal loading.

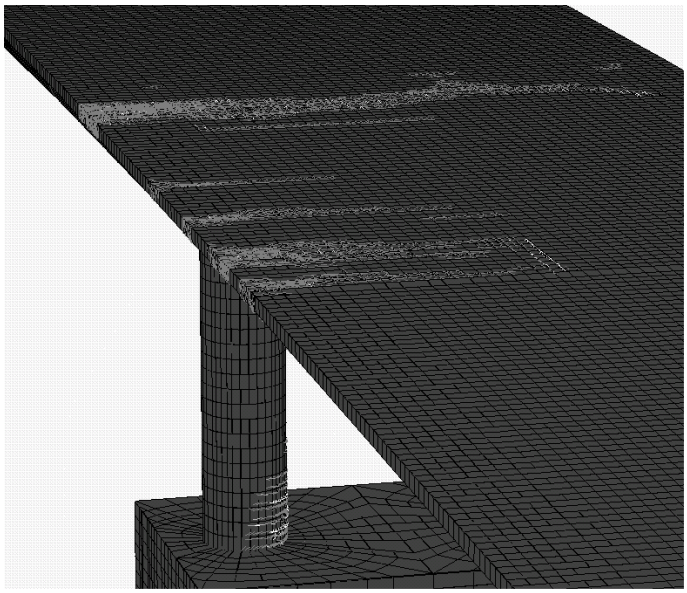

(A)

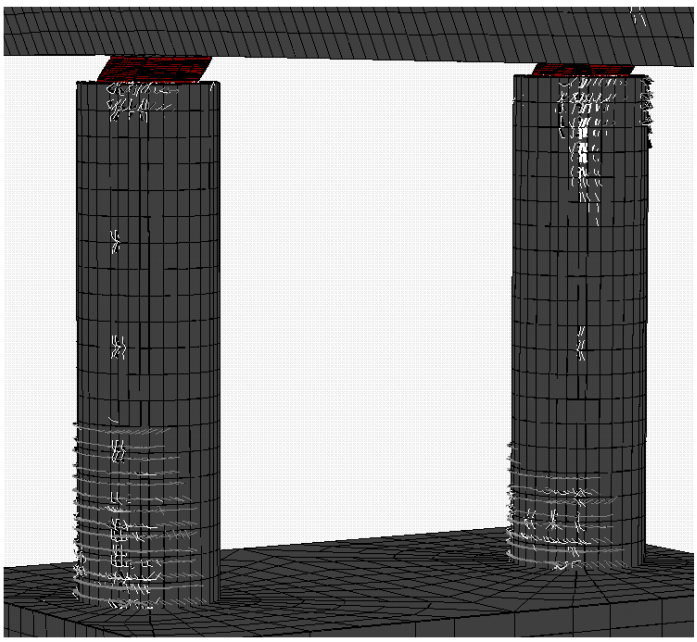

(B)

Figure 31. Crack patterns developed prior to failure. (A) Deck and (B) Piers of the bridge.

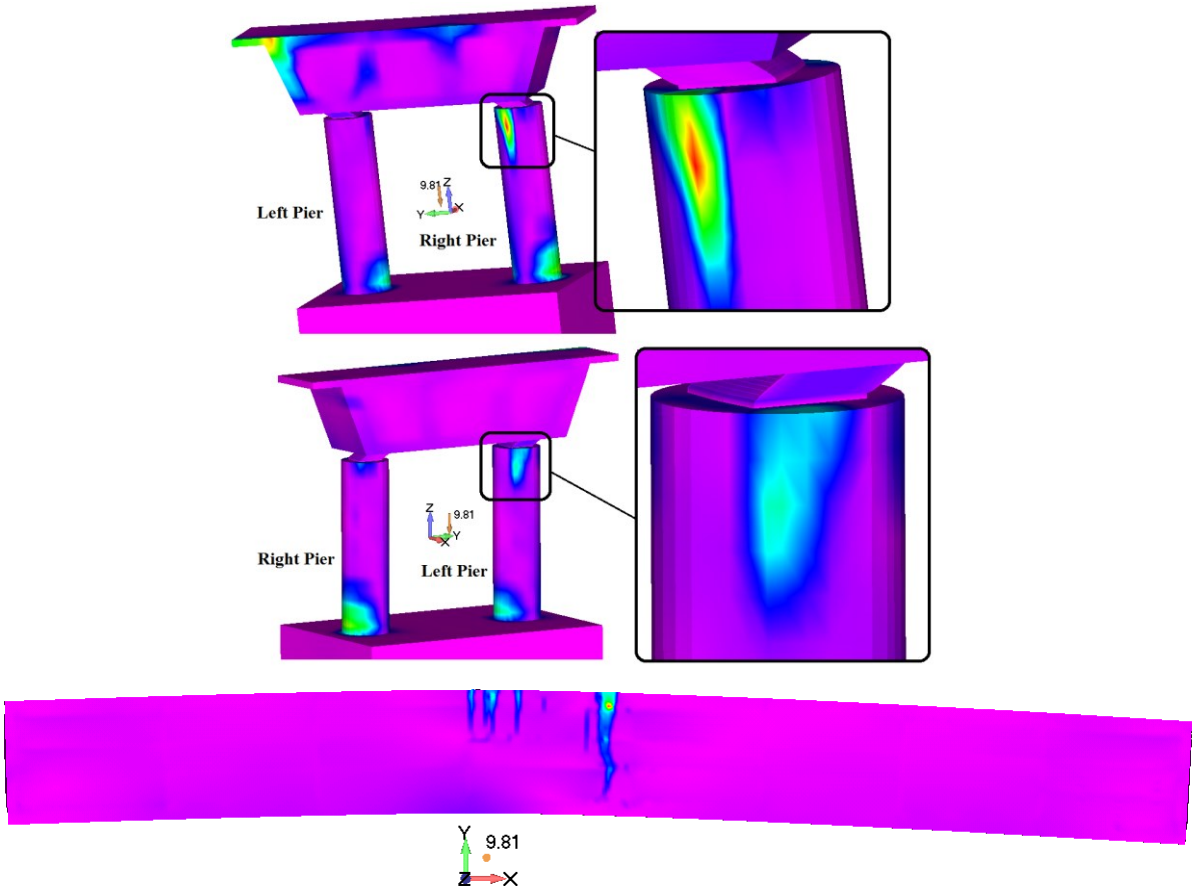

Figure 32. von Mises strain contours of the (Up) piers and middle vertical diaphragm and (Down) upper slab of the deck (seismic load direction: Y-axis).

As it can be seen in Fig. 31 the cracks that developed prior to failure are mainly located at the base and head of the piers, and the upper slab of the deck that is under tension due to the out-of-plane bending of the deck. Tensile cracks were also developed at the lower slab of the deck in a similar pattern as that shown in Fig. 31a & 32. The cracks that developed at the base of the piers are attributed to the bending moments that are generated due to the horizontal loads transferred from the bearings to the piers, while the diagonal cracks at the head of the two piers are attributed to shear and torsional deformations. This numerical finding illustrates the importance of using sufficient shear reinforcement so as to avoid any future vulnerability of these structural members (Fig. 32) during an earthquake excitation. For this reason many designers increase the diameter of the head of the piers so as to increase the shear resistance and avoid any local cracking. In this case, an increase of the piers heads is also proposed.

From the computational point of view, the total required computational time required to complete all numerical procedure was 46 hours and 30 minutes. 2.3% of the total computational time was attributed to the mesh generation procedure, while 26.5% was attributed to the output data writing process. As it can be depicted from Table 5, the nonlinear solution procedure requires almost 71% of the total computational time thus it is evident that it is the numerical procedure that derives the highest computation demands (mainly due to the stiffness inversion procedure – total number of stored stiffness matrix elements 798,697,535). It is also important to note here that the 33 hours required for the nonlinear solution procedure correspond to the numerical solution of a total of 100 internal iterations thus for the solution of each internal iteration it was required 19 minutes and 48 seconds.

a/a	Description	Value
1	Number of Hexahedral Elements	109,338
2	Number of Nodes (hexa8 only)	177,149
3	Number of Macro-Elements	49,172
4	Total Number of Embedded Rebar FEs Generated	529,332
5	Total Number of Short Embedded Rebar FEs that were Discarded by the Filter Algorithm	887
6	Required Embedded Mesh Generation Time	65 m 5 s
7	Required RAM for the Stiffness Matrix	5.95 Gb
8	Max Required RAM Allocated by the Software	20.65 Gb
9	Computational Time for Solving 10 Load Increment	33 hrs
10	Computational Time for Writing the Output Data	12 hrs 20m
11	Total Computational Time	46 hrs 30m

Table 5. General numerical details that derived after the nonlinear analysis of the complete FE model.

4 CONCLUSIONS

- The numerical investigation of the mechanical behavior of a full-scale RC bridge was performed through the use of 3D detailed analysis.
- The detailed mesh of the bridge was constructed through the use of 8-noded hexahedral elements that treat the cracking phenomenon through the smeared crack approach. The reinforcement grid is modeled through the use of embedded rod elements inside the hexahedral mesh.
- After performing the embedded mesh generation method [60] the derived results underline the importance of having a computationally efficient embedded rebar mesh generation techniques that will allocate large numbers of embedded rebars inside hexahedral meshes.
- A parametric investigation and a numerical calibration of the elastomeric bearings were performed so as to derive the optimum material parameters in modeling the exact geometry of the isolation system of the under study bridge.
- A simplified model was also constructed in SAP2000 so as to perform linear analysis and compare the numerical results that derived from the detailed model. As it was shown the deflection that resulted from the two models were close.
- Prestress was included in the 3D detailed model by incorporating an algorithm that provides the ability of assigning the posttension force at the tendons (which are also modeled as embedded rebar elements) as an initial force condition. The requirement in prestress resulted after performing a static nonlinear analysis for the dead loads of the 3D detailed model. Further investigation is required so as to verify the numerical performance of the prestress algorithm (comparison with experimental results of prestress beams, which will be the subject of future research work).
- The preliminary analysis revealed that the elastomeric bearings at the piers were underdesigned thus an increase of the initial area was proposed.
- The RC bridge was seismically assessed according to EC8, were it was found that the code's demand was satisfied. In addition to that, it was found that the bearings at the two

piers controled the failure mechanism of the bridge given that they are the structural members that fail first.

- Regarding the derived deformed shape and crack pattern of the bridge, it was found that the deck behaves in a similar manner to a beam that is under bending while rotation of the deck about the gravity axis (Z-axis) occurs due to the uneven spans. This rotation affects the deform shape of the piers, which crack at the base due to bending but develop shear deformations at the heads due to both shear forces and torsion that results from the deck's rotation. Avoiding the development of shear cracks at the heads of the piers during an earthquake excitation, an increase of the piers head's diameter is proposed.
- From the computational point of view, it was found that the nonlinear solution is the most computationally demanding procedure (71%), while the I/O for writing the output data required 26.5% of the total operational time. This illustrates the computational efficiency of the embedded mesh generation method (2.3%) thus underlines the requirement of using parallel processing for the computationally demanding stages of the at hand numerical problem. Nevertheless, the overall computational response of the software, illustrates the potential of solving this type of numerical problems in a very short period of time given the future advances in both hardware and compiling technology.
- The numerical limitations of using 3D detailed FE models, for analyzing the mechanical behavior of RC bridges, have been investigated. The numerical findings underline the importance of optimum algorithmic design and the use of accurate but efficient numerical models that will alleviate the significant problem of the computational demand when dealing with large-scale FE meshes. This type of modeling approach is ideal for assessing the design of any type of RC structures and the seismic or carrying capacity of existing RC structures. Given that the FEs used above can model any type of 3D geometry, the interaction with soil can also be accounted for.
- Future research work foresees the incorporation of a parallel solution algorithm for the nonlinear procedure, which was found to be the most time consuming numerical process.

REFERENCES

[1] CEN, prEN1998-2, EC8-2: Design provisions for earthquake resistance of structures. Part 2: Bridges, 2003.

[2] AASHTO LRFD, *AASHTO LRFD Bridge Design Specifications*, American Association of State Highway and Transportation Officials, Washington, D.C, 2007.

[3] R. Goel, A. Chopra, Nonlinear Analysis of Ordinary Bridges Crossing Fault-Rupture Zones, *Journal of Bridge Engineering*, **14**(3), 216–224, 2009.

[4] A.S. Elnashai, D.C. McClure, Effect of Modeling Assumptions and Input Motion Characteristics on Seismic Design Parameters of RC Bridge Piers, *Earthquake Engineering & Structural Dynamics*, **25**(5), 435–463, 1996.

[5] T.S. Paraskeva, A.J. Kappos, A.G. Sextos, Extension of modal pushover analysis to seismic assessment of bridges, *Earthquake Engineering & Structural Dynamics*, **35**(10), 1269–1293, 2006.

[6] T. Potisuk, C. Higgins, Field Testing and Analysis of CRC Deck Girder Bridge, *Journal of Bridge Engineering*, **12**(1), 53–63, 2007.

[7] H. Li, J. Wekezer, L. Kwasniewski, Dynamic Response of a Highway Bridge Subjected to Moving Vehicles, *Journal of Bridge Engineering*, **13**(5), 439–448, 2008.

[8] N. Johnson, M. Saiidi, D. Sanders, Nonlinear Earthquake Response Modeling of a Large-Scale Two-Span Concrete Bridge, *Journal of Bridge Engineering*, **14**(6), 460–471, 2009.

[9] W. Lee, S. Billington, Modeling Residual Displacements of Concrete Bridge Columns under Earthquake Loads Using Fiber Elements, *Journal of Bridge Engineering*, **15**(3), 240–249, 2010.

[10] A. Aviram, K.R. Mackie, B. Stojadinovic, Nonlinear Modeling of Bridge Structures in California, *ACI*, **271**, 1-26, 2010.

[11] Z.-C. Wang, W.-X. Ren, Dynamic Analysis of Prestressed Concrete Box-Girder Bridges by using the Beam Segment Finite Element Method, *International Journal of Structural Stability and Dynamics*, **11**(2), 379-399, 2011.

[12] P. Kaviani, F. Zareian, E. Taciroglu, Seismic behavior of reinforced concrete bridges with skew-angled seat-type abutments, *Engineering Structures*, **45**, 137–150, 2012.

[13] Y. Zhou, J. Prader, J. Weidner, N. Dubbs, F. Moon, A. Aktan, Structural Identification of a Deteriorated Reinforced Concrete Bridge *Journal of Bridge Engineering*, **17**(5), 774–787, 2012.

[14] A.J. Kappos, M.S. Saiidi, M.N. Aydinoglou, T. Isaković, *Seismic design and assessment of Bridges. Inelastic methods and case studies*, Springer, Geotechnical, Geological and Earthquake Engineering, 2012.

[15] P. Théoret, B. Massicotte, D. Conciatori, Analysis and Design of Straight and Skewed Slab Bridges, *Journal of Bridge Engineering*, **17**(2), 289–301, 2012.

[16] E.T. Filipov, L.A. Fahnestock, J.S. Steelman, J.F. Hajjar, J.M. LaFave, D.A. Foutch, Evaluation of quasi-isolated seismic bridge behavior using nonlinear bearing models, *Engineering Structures*, **49**, 168-181, 2013.

[17] I.F. Moschonas, A.J. Kappos, Assessment of concrete bridges subjected to ground motion with an arbitrary angle of incidence: static and dynamic approach, *Bulletin of Earthquake Engineering*, **11**(2), 581-605, 2013.

[18] A.Abdel-Mohti, G. Pekcan, Assessment of seismic performance of skew reinforced concrete box girder bridges, *International Journal of Advanced Structural Engineering*, **5**, 1-18, 2013.

[19] B. Richard, S. Epaillard, Ch. Cremona, L. Elfgren, L. Adelaide, Nonlinear finite element analysis of a 50 years old concrete trough bridge, *Engineering Structures*, **32**, 3899-3910, 2010.

[20] Ch.Ch. Chou, H.-J. Chang, J.T. Hewes, Two-plastic-hinge and two dimensional finite element models for post-tensioned precast concrete segmental bridge columns, *Engineering Structures*, **46,** 205–217, 2013.

[21] C.M. Frissen, M.A.N. Hendriks, N. Kaptijn, 3D Finite element analysis of Multi-beam Box girder Bridges – assessment of cross-sectional forces in joints, M.A.N. Hendriks, J.G. Rots, eds, *Third DIANA World Conference*, Tokyo, Japan 9-11 October, 2002.

[22] W. Kwan, S. Billington, Unbonded Posttensioned Concrete Bridge Piers. II: Seismic Analyses, *Journal of Bridge Engineering*, **8**(2), 102–111, 2003.

[23] J. Cervenka, W. Cervenka, Z. Janda, *Safety assessment of railway bridges by non-linear analysis*, In: Bien, Elfgren, Olofsson eds, Sustainable bridges, Wroclaw, DWE, 2007.

[24] Z. Sun, B. Si, D. Wang, X. Guo, Experimental research and finite element analysis of bridge piers failed in flexure-shear modes, *Earthquake Engineering and Engineering Vibration*, **7**(4), 403-414, 2008.

[25] V.K. Papanikolaou, A.J. Kappos, Numerical study of confinement effectiveness in solid and hollow reinforced concrete bridge piers: Part 1: Methodology and Part 2: Analysis results and discussion. *Engineering Structures*; **87**, 1427–1439, 1440-1450, 2009.

[26] T.L.T. Nguyen, P.F. Silva, M.T. Manzari, A. Belarbi, System Modeling for Seismic Performance Assessment and Evaluation of Reinforced Concrete Bridge Columns, *ACI*, **271**, 125-146, 2010.

[27] Y. Sha, H. Hao, Nonlinear finite element analysis of barge collision with a single bridge pier, *Engineering Structures*, **41**, 63-76, 2012.

[28] R. Chacon, E. Mirambell, E. Real, Strength and ductility of concrete-filled tubular piers of integral bridges, *Engineering Structures*, **46**, 234–246, 2013.

[29] Y. Deng, G. Morcous, Efficient Prestressed Concrete-Steel Composite Girder for Medium-Span Bridges: II - Finite Element Analysis and Experimental Investigation, *Journal of Bridge Engineering*, In Press, 2013.

[30] P. Zhu, M. Abe, Y.Fujino, Modelling three-dimensional non-linear seismic performance of elevated bridges with emphasis on pounding of girders, *Earthquake Engineering & Structural Dynamics*; **31**, 1891–1913, 2002.

[31] Z. Ma, S. Chaudhury, J. Millam, J. Hulsey, Field Test and 3D FE Modeling of Decked Bulb-Tee Bridges, *Journal of Bridge Engineering*, **12**(3), 306–314, 2007.

[32] X.H. He, X.W. Sheng, A. Scanlon, D.G. Linzell, X.D. Yu, Skewed concrete box girder bridge static and dynamic testing and analysis, *Engineering Structures*, **39**, 38–49, 2012.

[33] K. Bi, H. Hao, Numerical simulation of pounding damage to bridge structures under spatially varying ground motions, *Engineering Structures*, **46**, 62-76, 2013.

[34] E.K.C. Tang, H. Hao, Numerical simulation of a cable-stayed bridge response to blast loads, Part I: Model development and response calculations, Part II: Damage prediction and FRP strengthening, *Engineering Structures*, **32**, 3180-3192, 3193-3205, 2010.

[35] A. Mwafy, O.-S. Kwon, A. Elnashai, Seismic assessment of an existing non-seismically designed major bridge-abutment-foundation system, *Engineering Structures*, **32**, 2192-2209, 2010.

[36] CSI, SAP2000 structural analysis program. Berkeley (California): Computers and Structures Inc; 2006. www.csiberkeley.com

[37] SC Solutions, Inc., California, Seismic Evaluation of the Cooper River Bridge, ADINA Tech Briefs, 2006. www.adina.com/newsgD4.shtml

[38] Elnashai AS, Papanikolaou V, Lee D. ZEUS-NL a system for inelastic analysis of structures. Urbana (IL): Mid-America Earthquake Center, University of Illinois at Urbana-Champaign; 2008.

[39] V. Cervenka, L. Jendele, J. Cervenka, *ATENA Program Documentation, Part 1: Theory*, Prague; 2008. www.cervenka.cz

[40] LS-DYNA. LS-DYNA user manual. Livermore Software Technology Corporation, 2007. www.ls-dyna.com

[41] S. Lan, J.E. Crawford, K.B. Morrill, Design of reinforced concrete columns to resist the effects of suitcase bombs. *In: Proceedings of the 6th Asia-Pacific Conference on Shock & Impact Loads on Structures*, pp. 325-332, 2005.

[42] GT STRUDL, Structural Design & Analysis Software. www.gtstrudl.gatech.edu

[43] ANSYS, *Release 11.0 Documentation for ANSYS*, ANSYS help, 2009. www.ansys.com

[44] Abaqus FEA, Simulia - Dassault Systèmes, 2010. www.3ds.com

[45] TNO Diana BV, *User's Manual*, 2011. http://tnodiana.com/

[46] Strand7, Using Strand7 Manual, Strand7 Pty Ltd, 2010. www.strand7.com

[47] DRAIN-3DX, Static and Dynamic Analysis of Inelastic 3D Structures, 2011.

[48] McKenna F, Fenves GL, Scott MH. Open system for earthquake engineering simulation. California: University of California Berkeley; 2000. http://opensees.berkeley.edu

[49] ADINA for structural analysis, User's Manual, ADINA R&D, Inc. www.adina.com

[50] H. Hartl, Development of a Continuum-Mechanics-Based Tool for 3D Finite Element Analysis of Reinforced Concrete Structures and Application to Problems of Soil-Structure Interaction, *Ph.D. Thesis, Graz University of Technology, Institute of. Structural Concrete*; 2002.

[51] M.D. Kotsovos, M.N. Pavlovic, *Structural concrete – finite-element analysis for limit-state design*, Thomas Telford Publications; 1995.

[52] C. Girard, J. Bastien, Finite Element bond slip model for concrete columns under cyclic loads, *Journal of Structural Engineering, ASCE*, **128**(12), 1502–1510, 2002.

[53] Mirzabozorg H, Ghaemian M. Nonlinear behavior of mass concrete in 3d problems using a smeared crack approach, *Earthquake Engineering & Structural Dynamics*, **34**, 247–269, 2005.

[54] G.C. Lykidis, K.V. Spiliopoulos, 3D Solid Finite-Element Analysis of Cyclically Loaded RC Structures Allowing Embedded Reinforcement Slippage, *Journal of Structural Engineering*, **134**(4), 629-638, 2008.

[55] L. Jendele, J. Cervenka, V. Saouma, R. Pukl, On the choice between discrete or smeared approach in practical structural FE analyses of concrete structures, CERVENKA CONSULTING, Predvoje 22, 16200 Prague 6, Czech Republic and CEAE Dep., University of Colorado at Boulder, USA.

[56] G. Markou, *Modeling of Reinforced Concrete Structures*, LAP Lambert Academic Publishing, 2011.

[57] G. Markou, M. Papadrakakis, An efficient generation method of embedded reinforcement in hexahedral elements for reinforced concrete simulations, *Advances in Engineering Software ADES*, **45**(1), 175-187, 2012.

[58] G. Markou and M. Papadrakakis, Modeling of Reinforced Concrete Structures with 3d detailed finite element models, *AHU Journal of Engineering and Applied Sciences*, **4**(2), 47-63, 2012.

[59] ReConAn FEA Analysis software, 2011. http://alhosnu.ae/Markou/index_files/ReConAn.htm

[60] G. Markou, Generating Embedded Rebar Elements for Large-Scale RC Models, M. Papadrakakis, M. Kojic, I. Tuncer eds., SEECCM III, 3rd South-East European Conference on Computational Mechanics, an ECCOMAS and IACM Special Interest Conference Kos Island, Greece, 12–14 June, 2013.

[61] G. Markou, Embedded reinforcement mesh generation method for large-scale RC simulations: Case study, *AHU Journal of Engineering & Applied Sciences*, **5**(1), 23-42, 2012.

[62] G. Markou and M. Papadrakakis, An efficient generation method of embedded reinforcement in hexahedral elements for reinforced concrete simulations, *Advances in Engineering Software ADES*, **45**(1), 175-187, 2012.

[63] Ch.D. Newhouse, S.A. Bole, W.R. Burkett, P.T. Nash, M. El-Shami, Study of Elastomeric Bearings for Superelevated U-Beam Bridges, *Research Report*, *Texas University*, October, 2009.

[64] R.A. Cook, D.T. Allen, M.H. Ansley, Stiffness Evaluation of Neoprene Bearing Pads under Long-Term Loads, *Research Report, University of Florida*, March, 2009.

[65] J. Wekezer, E. Taft, L. Kwasniewski, S. Earle, Investigation of impact factors for FODT bridges. FDOT Structures research laboratory final report, *Research Report, University of Florida*, December, 2010.

[66] Australian Standards, AS 5100.4 SUPP 1-2006 bridge design - bearings and deck joints, Standards Australia, 2006.

[67] VSL, CTT Elastomeric Bearings. www.vsl.com/document.php?getfile=2719

[68] G. Stavroulakis, M. Papadrakakis, Advances on the domain decomposition solution of large scale porous media problems, *Computer Methods in Applied Mechanics and Engineering*, **196**, 1935-1945, 2009.